Exploring the electron + track signature to measure tau g-2

Siemen Aulich, University of Göttingen, Germany

September 4, 2024

Abstract

The anomalous magnetic moment describes the deviation of magnetic moment from a value of 2. The deviation arises from loop corrections to the lepton coupling to the photon field. While the anomalous magnetic moment of the electron, is one of the most precisely measured values in physics, the anomalous magnetic moment of the tau is only poorly measured. Due to the tau's higher mass compared to the other leptons, its anomalous magnetic moment is a sensitive marker for beyond standard model effects. This work engages in the analysis of the tau's anomalous magnetic moment by examining ultra-peripheral collisions of lead ions at the LHC. The process is accessed by examining decays to electrons and hadrons of the tau. The analysis is based on the ATLAS detector at the LHC. The event selection is optimised to suppress background processes. The sensitivity of the analysis is estimated by a likelihood scan of Asimov data. The analysis is expected to provide a competitive measurement of the tau's anomalous magnetic moment.

Contents

1 Introduction

Historically the electron's spin was one of the first manifestation of quantum mechanics. The first observation of the electron's spin was made by Stern and Gerlach in 1922. They observed that a beam of silver atoms was split into two beams when passing through an inhomogeneous magnetic field. This was explained by the magnetic moment of the electron's spin. The spin magnetic moment of the electron was found to be proportional to its spin. The proportionality factor is called the g-factor. The Dirac equation predicted the value of the g-factor to be exactly 2. However, the g-factor of the electron was measured to slightly deviate from 2. The deviation from a value of 2 is called anomalous magnetic moment. In the framework of quantum field theories this deviation is explained by higher order corrections in the coupling of the electron in the photon field. Nowadays, the anomalous magnetic moment of the electron is measured to agree with its prediction to over 10 significant digits. Making it one of the most precisely measured quantities in physics.

With the discovery of the other leptons, namely the muon and tau, their anomalous magnetic moment became of interest too. Due to the different mass, their anomalous magnetic moments diverge from the electron's. Precision measurements of the muon's anomalous magnetic moment revealed possible deviation from the standard model prediction. While the muon's magnetic moment can be measured by examining its spin precision in a storage ring. Due to the short lifetime of the tau, a different approach is needed to measure its anomalous magnetic moment. The tau's magnetic moment can be measured by examining its coupling to photons.

The most precise measurement of the tau's anomalous magnetic moment was achieved by the DELPHI experiment at LEP around 20 years ago. The measurement was based on radiative diphoton production of tau pairs. This work engages in the analysis of the tau's anomalous magnetic moment by examining ultra-peripheral collisions of lead ions at the LHC. Strong electro magnetic fields generated by the lead ions generate a suitable environment to study the tau's coupling to photons.

2 Theory

2.1 Anomalous magnetic moment

The g-factor of a particle is defined via the porportionality of the spin angular momentum $\vec{S}$ of the particle to the magnetic moment μ of the particle

$$\vec{\mu} = g\frac{q}{2m}\vec{S} \tag{1}$$

where q is the charge of the particle, m is the mass of the particle.

The Dirac equation predicts the g-factor of the leptons to be exactly $g = 2$ [1].

In the framework of quantum field theory, the g-factor of the leptons is corrected by higher order corrections. These corrections can be described by summing up loop diagrams contributing to the coupling of the lepton to the photon field [2]. This process yields a power series in the coupling parameters of the theory. A detailed description of the calculation

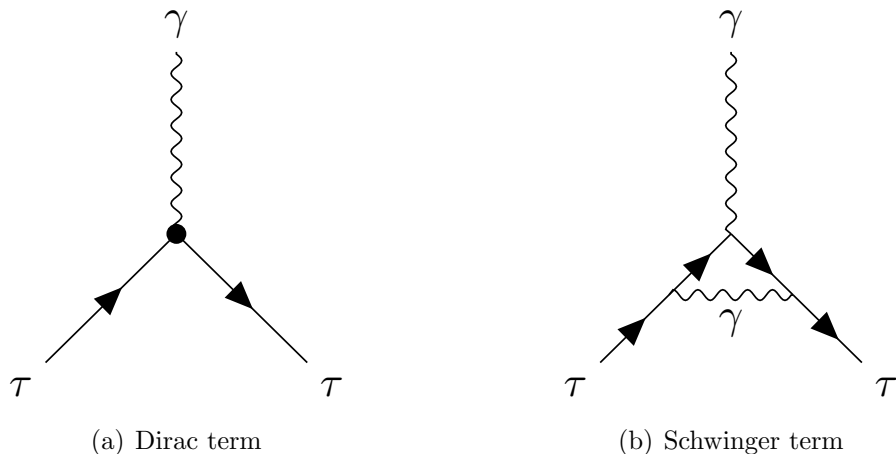(a) Dirac term   (b) Schwinger term

Figure 1: Feynman diagrams showing the leading order QED contributions to the tau's anomalous magnetic moment.

would exceed the scope of this work.

Exemplary diagrams contributing to the anomalous magnetic moment of the tau are shown in Figure 1.

The deviation of the g-factor from 2 is called anomalous magnetic moment. The anomalous magnetic moment is defined as

$$a_\ell = \frac{g_\ell - 2}{2} \, . \tag{2}$$

The anomalous magnetic moment of the electron is measured to be $a_e = 0.00115965218128(53)$ [3]. This value agrees with the theoretical prediction [4] to over 10 significant digits.

The anomalous magnetic moment of the muon is measured to be $a_\mu = 0.116592057(25)$ [5]. In contrast to the electron, the muon's magnetic moment is significantly influenced by QCD contribution. These render the theoretical prediction of the muon's magnetic moment less precise.

The tau's anomalous magnetic moment is predicted to be $a_\tau = 0.00117721(5)$ [6]. The tau's anomalous magnetic moment is less precisely measured than the electron's and muon's. The most precise measurement of the tau's anomalous magnetic moment was achieved by the DELPHI experiment at LEP. The measurement was based on radiative diphoton production of tau pairs. The measurement yielded a value of $a_\tau = 0.0115(17)$ [7].

2.2   Ultra-peripheral collisions

Ultra-peripheral collisions are a special type of collisions where the impact parameter of the colliding particles is larger than the sum of their radii. In this case the particles scatter elastically and interaction between the particles is dominated by photon exchange. The high Z of the lead ions generates strong electromagnetic fields. The photons can produce tau pairs via the process shown in Figure 2. This process is sensitive to the tau's magnetic moment.
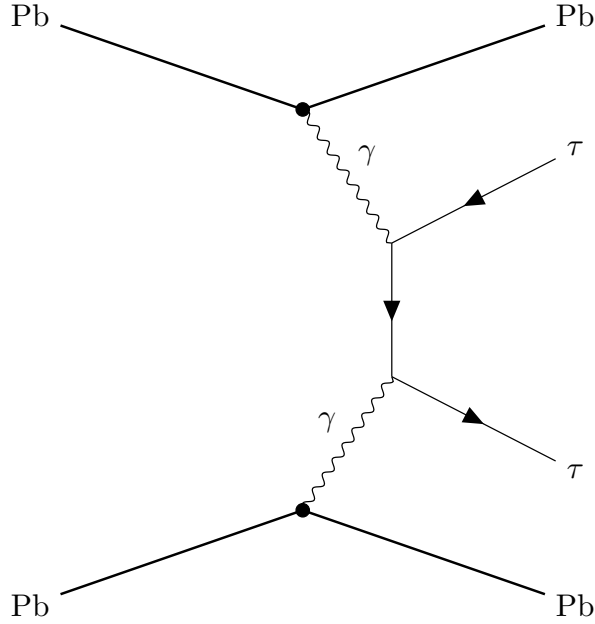
Figure 2: Feynman diagram showing the ultra-peripheral collision of lead ions producing tau pairs.

2.3 Tau Decays

Name	Decay mode	Branching ratio
Leptonic	$\tau^{\pm} \to \ell^{\pm} \bar{\nu}_{\ell} \nu_{\tau}$	35%
1 Prong	$\tau^{\pm} \to \nu_{\tau} \pi^{\pm} +$ neutral hadrons	46%
3 Prong	$\tau^{\pm} \to \nu_{\tau} \pi^{\pm} \pi^{\pm} \pi^{\mp} +$ neutral hadrons	19%

Table 1: Decay modes of the tau lepton. The branching ratios are taken from [8].

Tau leptons exclusively decay via the weak interaction. It decays to leptons and hadrons, with hadrons primarily being pions. The decay modes of the tau lepton are shown in Table 1. For future reference the decay modes are named as leptonic, 1 prong and 3 prong decay, where the number refers to the number of charged pions in the final state.

2.4 Sensitivity of a_{τ} to New Physics

The loop corrections to the anomalous magnetic moment make it sensitive to contributions by beyond standard model (BSM) effects. The contributions of BSM effects are expected to scale according to [9]

$$\delta a_{\tau} \propto \frac{m_{\ell}^2}{M_X^2} \tag{3}$$

where M_X denotes the mass of a potential BSM particle and m_{ℓ} the lepton's mass. This makes the tau potentially 280 times more sensitive than the muon.

3 Experimental Setup

3.1 The LHC

The Large Hadron Collider (LHC) at CERN is a synchrotron designed to accelerate protons and lead nuclei. This work focuses on the Pb-Pb collisions during Run 3. During Run 3 from 2022 to 2025, the LHC collides lead ions at a center of mass energy of $\sqrt{s} = 5.02\,\mathrm{TeV}$. The lead ions are accelerated to an energy of $5.36\,\mathrm{TeV}$ per nucleon. For the full Run 3 an integrated luminosity of $6\,\mathrm{nb^{-1}}$ is expected [10].
After completion of Run 3 in Dec. 2025 and an operational pause, the LHC will operate with increased luminosity as the High-Luminosity Large Hadron Collider (HL-LHC). During this time period, it is expected to accumulate an integrated luminosity of $20\,\mathrm{nb^{-1}}$ [10].

3.2 The ATLAS Detector

The ATLAS detector is a general purpose detector at the LHC. It can roughly be separated into three elements: the inner detector, the calorimeter and the muon spectrometer [11].

3.3 The Inner Detector

The inner detector of the ATLAS detector is designed to measure the tracks of charged particles. It is closest to the beam pipe. The inner detector is encapsulated by a solenoid magnet. The magnetic field allows for a measurement of the transverse momentum of charged particles. It consists of three components, the pixel detector, the semiconductor tracker (SCT) and the transition radiation tracker (TRT). The pixel detector is the closest to the beam pipe. It consists of three layers of pixel sensors. The SCT is the second layer of the inner detector. It consists of silicon strip sensors. The TRT is the outermost layer of the inner detector. It consists of straw tubes filled with a gas mixture. The TRT is used to measure the track of low momentum.

3.4 The Calorimeter

The calorimeters are the detector elements following the inner detectors. They are meant to (destructively) measure a particle's energy. As for the central part of the detector, the calorimeter is divided into the electromagnetic calorimeter (ECAL) and the hadronic calorimeter (HCAL). The ECAL is designed to measure the energy of electrons and photons. It consists of lead and liquid argon. The HCAL is designed to measure the energy of hadrons. It consists of steel and scintillating tiles. The zero degree calorimeter (ZDC) is a special calorimeter designed to measure the energy of particles emitted at close to zero degree. It is located roughly at 140 meters from the interaction point and serves the purpose of measuring energy of uncharged hadrons.

3.5 The Muon Spectrometer

The muon spectrometer is the outermost part of the ATLAS detector. It is designed to measure the tracks of muons. The muon spectrometer consists of three parts, the monitored drift tubes (MDT), the cathode strip chambers (CSC) and the resistive plate chambers (RPC). The MDT is the innermost part of the muon spectrometer. It utilises a magnetic field that is differently oriented than the magnetic field of the inner detector to deliver a full momentum measurement of muons. The far outside location of the muon spectrometer ensures that only muons can reach it. Allowing for a clean reconstruction of muons.

3.6 The Trigger System

The LHC's bunch crossing rate is $40\,\mathrm{MHz}$. As this exceeds the readout capabilities of the detector, a trigger system is operated to reduce the amount of data to be read out. The trigger system consists of a hardware trigger and a software trigger. With the combination of both triggers, the data rate is reduced to $1\,\mathrm{kHz}$.

4 Event Selection

Observable	Preselection					
GRL	Pass					
$E_{\mathrm{ZDC}}^{A,C}$	< 1 TeV					
Trigger	passed_HLT					
Region	SR-1μ1T	SR-1e1T	SR-1μ3T	SR-1e3T	SR-1μ1e	CR-2ℓ
$N_\mu^{\mathrm{baseline}}$	=1	-	=1	-	-	-
N_μ^{sig}	=1	=0	=1	=0	=1	($= 2$)
N_e^{sig}	=0	=1	=0	=1	=1	($= 2$)
$N_{trk}(\Delta R > 0.1$ from $\mu^{sig})$	=1	=1	=3	=3	-	-
$N_{trk}(\Delta R > 0.1$ from $\ell^{sig})$	-	-	-	-	=0	=0
Unmatched clusters	=0	=0	=0	=0	-	-
$\sum$ charge	=0	=0	=0	=0	=0	-
$p_T^{(\mu,\mathrm{trk})}$	> 1 GeV	> 1 GeV	-	-	-	
$p_T^{(\mu,\mathrm{trk}),\gamma}$	> 1 GeV	> 1 GeV	-	-	-	
$p_T^{(\mu,\mathrm{trk}),\mathrm{cluster}}$	> 1 GeV	> 1 GeV	-	-	-	
m_{trks}	-	-	< 1.7 GeV	$\in [0.5$ GeV$, 1.7$ GeV$]$	-	-
$A^{\mu,\mathrm{trk(s)}}$	< 0.4	> 0.012	< 0.2	-	-	-
$m_{\mu\mu}$	-	-	-	-	-	$> 11 GeV$

Table 2: Event selection criteria for the signal and control regions.

The detailed event selection requirements are shown in Table 2. The event selection is divided into a preselection applying to all regions and region specific selections.

4.1 Preselection

The preselection requires the event to pass the good run list (GRL) requirements. To suppress the contribution from hadronic interactions in general, and photonuclear background in particular, the energy deposited in the zero degree calorimeters is required to be below 1 TeV. This is done, as the signal process involve no nuclear breakup, which would result in neutrons being emitted in the forward direction. The event is further required to pass the high level trigger (HLT) requirements. Note, that these differ for the electron and muon channels.

4.2 Signal Regions

The signal regions are labelled by the number of leptons and charged tracks in the event. They are defined to resemble possible combinations of τ decays, as shown in Table 1, while minimising contributions of background processes. The signal regions and the particle numbers are defined in Table 2.

A common feature, that is shared among all signal regions is the so-called charge-veto. It requires the total charge of the event to be zero. This is done to suppress background processes, that feature a non-zero charge in the final state.

Further, for all regions composed of tracks, a requirement on zero unmatched clusters is imposed. This is done to suppress background processes, e.g. hadronic processes, that feature clusters not associated to tracks.

5 Background

5.1 Photonuclear Background

Photonuclear processes are one possible source of background as they feature a low particle activity in the detector similar as the background process. Using the event selection outlined in Section 4 the photonuclear background is sufficiently suppressed, as shown in the previous analysis by ATLAS [12]. Therefore, the photonuclear background is not considered in this analysis.
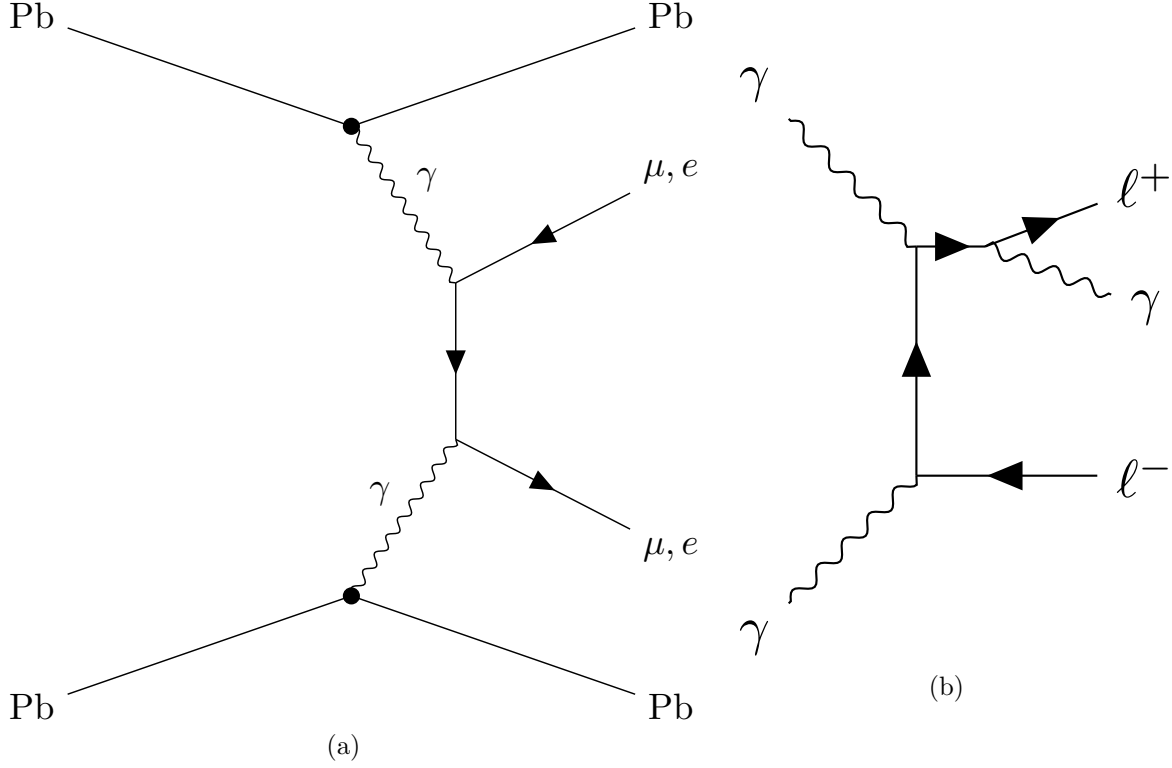
5.2 Exclusive dilepton production

Figure 3: Schematic diagram showing the exclusive dilepton production in ultraperipheral lead-lead collisions in (a). Final state radiation of photons in the dilepton process in (b).

In close resemblance of the signal process, the exclusive dilepton production of electron or muon pairs in ultra-peripheral collision via light-by-light scattering is the dominant background process. A schematic depiction of the process is shown in Figure 3(a). The signature of the process is characteristic by the presence of two leptons in the final state with otherwise low particle activity. The process can exhibit final state radiation (FSR) of photons. This leads to a stronger resemblance of the signal process.

5.3 Exclusive Dilepton Production with ρ^0 Decays

Another possible background stems from the simultaneous production of a ρ^0 meson and a dilepton pair. The ρ^0 meson can be produced via

$$\gamma A \to \rho^0 \to \pi\pi \,.$$

The SR-1ℓ3T regions are particularly susceptible to this background, as the ρ^0 can decay to three charged pions. As it was shown in ??, the background is sufficiently suppressed by the event selection criteria.

6 Evaluation of the Event Selection

The detailed cutflows for each region can be found in Appendix A. Note, that as some background apparent in the data is not simulated and the ZDC cut is not simulated in the Monte Carlo samples but only applied as a weight, some deviations between prediction and data in the cutflow are expected.
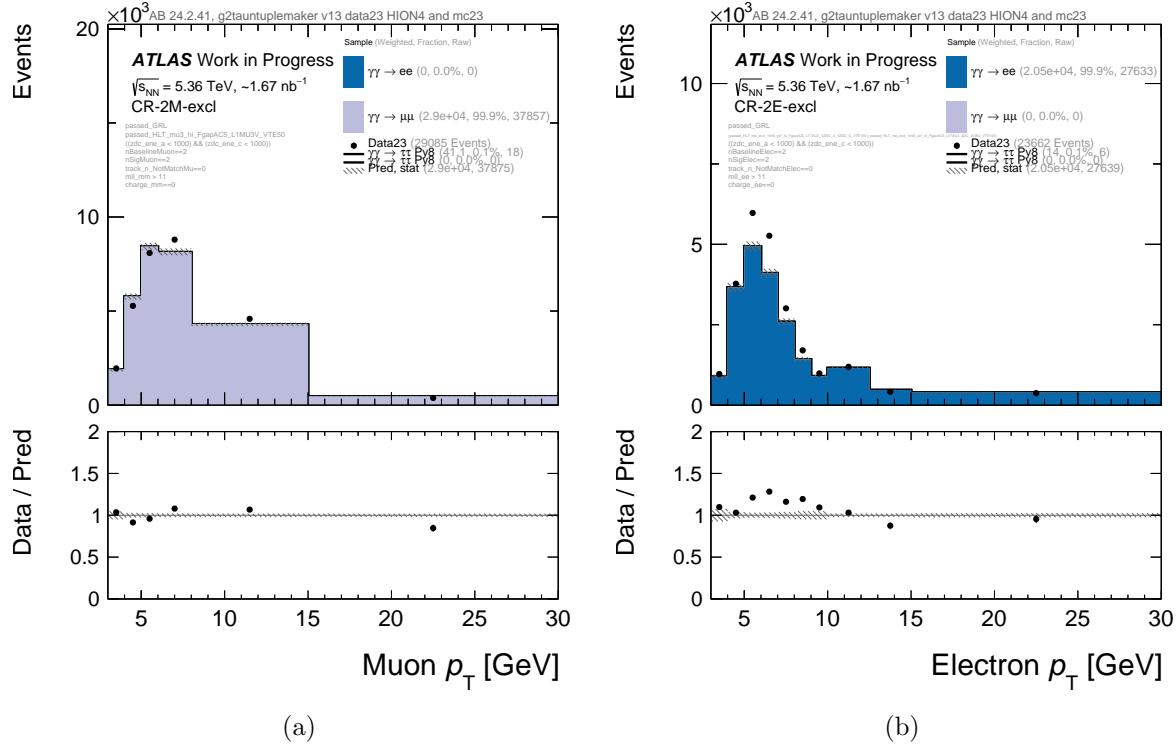
6.1 CR-2ℓ

Figure 4: Transverse momentum of muon (a) and electron (b) in the CR-2ℓ regions.

The cutflow for the CR-2ℓ regions do not show any particularly interesting feature. It can be seen, that while for the CR-2μ region prediction and data agree well, the CR-2e regions shows a deviation in the expected yield of $\sim 13\%$. The distributions of the transverse momentum of the muon and electron in the CR-2ℓ regions are shown in Figure 4. The agreement of the data and the prediction matches well for CR-2μ, while for the CR-2e region the prediction is slightly below. The ratio of prediction to data reveals, that the deviation is not uniform over the whole p_T range. However, in the high statistics bins, the ratio between prediction and data appears to be consistent with unity. It should be noted, that the prediction was run with a lower number of events in the Monte Carlo samples, than what is aspired for the final analysis. This could lead to a statistical fluctuation in the prediction.
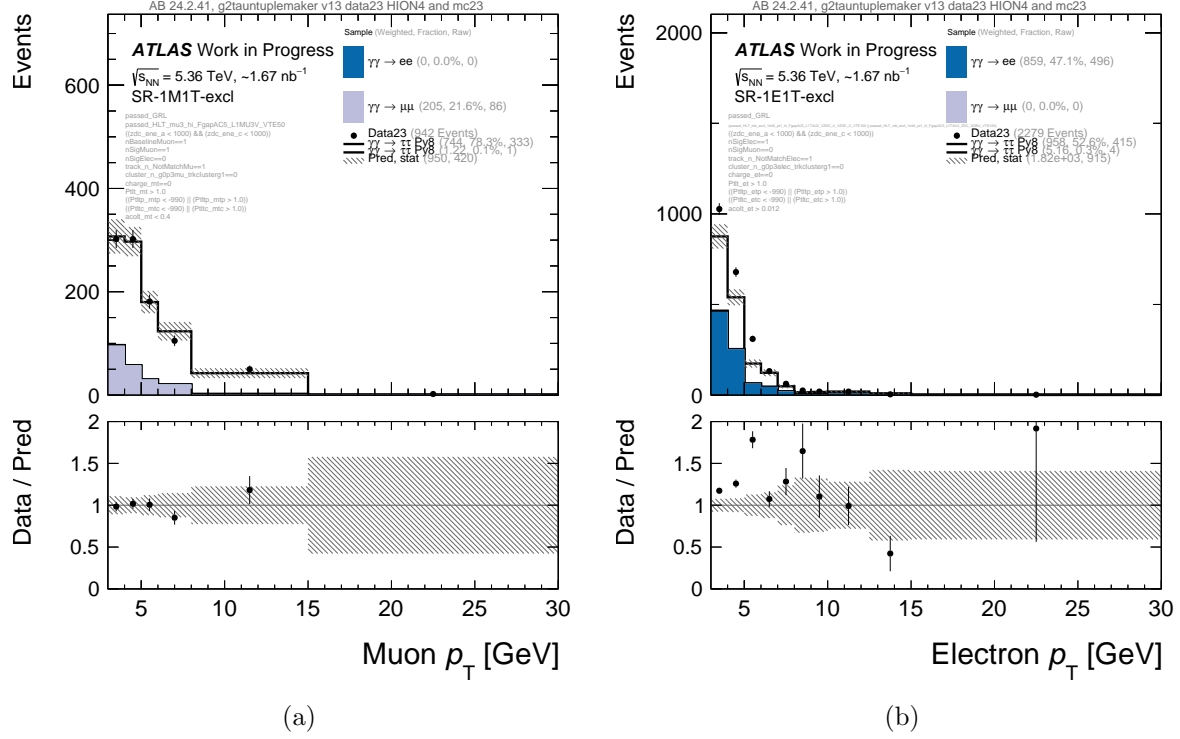
6.2   SR-1ℓ1T

Figure 5: Transverse momentum of muon (a) and electron (b) in the SR-1ℓ1T regions.

The SR-1ℓ1T regions are defined by the presence of one lepton and one charged track. This makes the region the most susceptible to the contribution of the dilepton background. It can be seen, that up until the charge-veto the signal to background ratio is very low in both regions. For the charge-veto cut, the SR-1e1T regions shows more than 10 times more background than SR-1μ1T. Such a behaviour is explained by the better reconstruction performance for muons, making the region less susceptible to leptons from dilepton background failing the muon identification. This is further supported by the baseline muon identification, where the background can be significantly reduced by requiring only one baseline muon. Such a selection is absent for the electron regions.

For the SR-1μ1T region, the signal-to-background ratio is significantly improved by the requirement of $p_T^{\mu,\mathrm{trk}} > 1$ GeV. This is due to the fact, that the signal process features a non-collinear lepton and track system, caused by the irradiation of a neutrino. This is different for the dilepton background, where the leptons are collinear. In the case of the SR-1e1T region, the signal-to-background ratio is only slightly improved by the requirement of $p_T^{e,\mathrm{trk}} > 1$ GeV. While for SR-1μ1T, the background is reduced by a factor of 10, the reduction for SR-1e1T is below a factor of 2.

The cuts on $p_T^{(e,\mathrm{trk},\gamma)}$ or $p_T^{(e,\mathrm{trk,cluster})}$ further reduce the contribution of the dilepton background for both regions. The impacts have a higher impact in the electron region, which

---

[0]The baseline muon identification is a less strict requirement for the identification of a muon, allowing for the identification of lower p_T muons.

is, given the higher background remaining at this point in the cutflow, expected. Lastly the cut on the acoplanarity $A_\phi^{e,\mathrm{trk}} > 0.012$ reduce the background in the SR-1e1T region by a factor of 20. For the SR-1μ1T region, the cut has a no significant impact on the background (or the signal).

In total, the SR-1e1T region has almost 4 times the background of the SR-1μ1T region. This is due to the better reconstruction performance of muons compared to electrons. The distributions of the transverse momentum of the muon and electron in the SR-1ℓ1T regions are shown in Figure 5. The agreement of the data and the prediction is very good for the SR-1μ1T region, with all bins being inside the uncertainty of the prediction. For the SR-1e1T region, some disagreement is visible across the whole p_T range. The ratio of prediction to data varies across the bin, showing a deviation from unity. Thus, the deviation may not only be due to a faulty normalisation. It is however to be noted, that the deviation of the normalisation of the dilepton background, as seen in CR-2e, is expected to also affect the SR-1e1T region.

6.3 SR-1ℓ3T
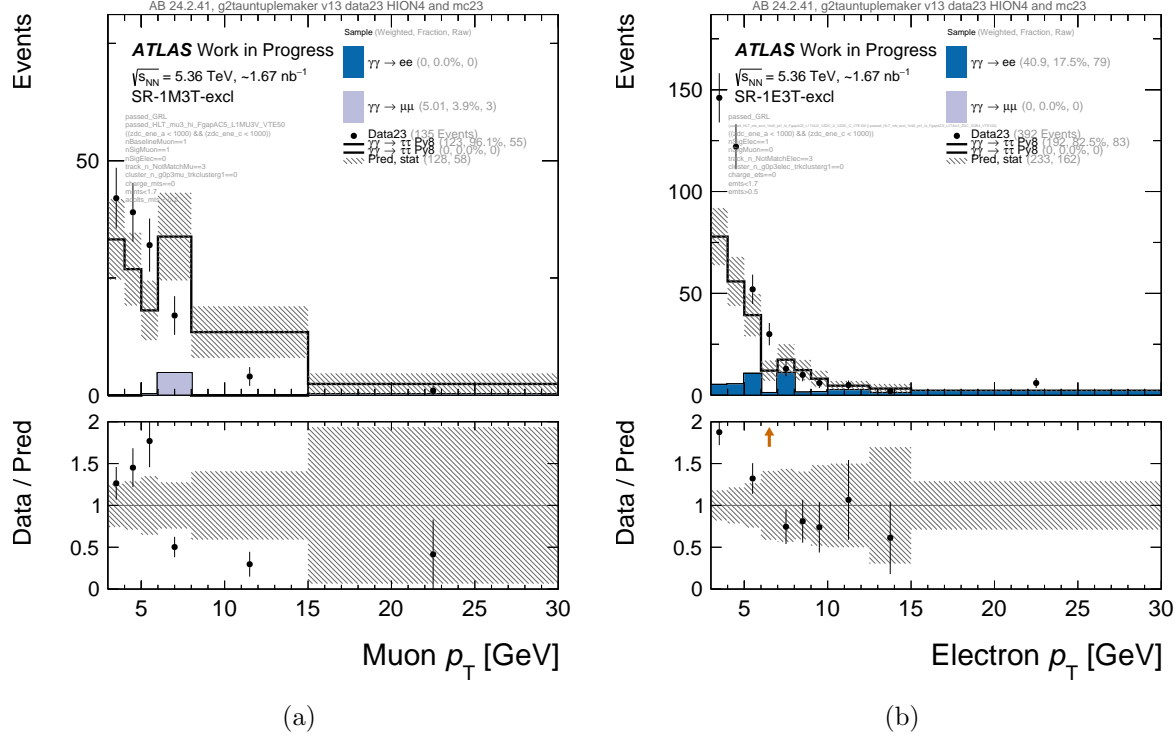

Figure 6: Transverse momentum of muon (a) and electron (b) in the SR-1ℓ3T regions.

For both the SR-1μ3T and SR-1e3T regions, the background yield decreases rapidly after following the $N_{trk}(\Delta R > 0.1$ from $\ell) = 3$ cut. This is due to the fact, that the dilepton process itself is not expected to produce three charged tracks. FSR of photon and photon conversion can, however, lead to the presence of three tracks. This makes this region a lot cleaner in comparison to the SR-1ℓ1T regions.

The cluster-veto has little impact on the background, but reduces the yield in the data sample. This effect is ascribed to background that have not been simulated, e.g. hadronic interactions.

The cut on the invariant mass of the tracks m_{trks} again is of low impact on the background. For the data sample, it reduces the yield by a factor of 2. This behaviour is mostly explained by the simultaneous production of ρ^0 mesons and dilepton pairs (See Section 5.3).

In total, for the SR-1μ3T region the prediction of the yields agrees with the data well. As for the shape of the distribution as seen in Figure 6(a) for the transverse momentum, however, deviation can clearly be seen. Due to the low statistics of the region and the simulation process, these should mostly be attributed to statistical fluctuations.

For the SR-1e3T region, the prediction is exceeded by the data by $\sim 68\%$. Figure 6(b) shows the distribution of the transverse momentum. The deviation is not uniform over the whole p_T range, but is most prominent in the low p_T bins.

As described before the lower identification efficiency for electrons, increase the background contribution in the SR-1e3T region. This also applies to the ρ^0 meson background. In [12] it was shown, that the ρ^0 meson background is significantly reduced by the m_{trks} cut. This analysis, however, took only the muon regions into account. Offering a possible explanation for the deviation in the SR-1e3T region. Figure 12 shows the distribution of the invariant mass of the tracks in SR-1ℓ3T before applying the m_{trks} cut. For the electron region, the data shows a continuous background, that is not included in the prediction. This background is not present in the muon region. This background is most likely due to the ρ^0 meson background. A possible way to investigate this, would be examining the distribution of the invariant mass of the two subleading tracks in the ρ^0 mass window. If the contribution stems from the ρ^0 meson background, the distribution should peak at the ρ^0 mass. As this variable was not included in the ntuples at this point, this investigation is left for future work.

6.4 SR-1μ1e

The requirement of having both a muon and an electron in the final state, grants the SR-1μ1e region a very high robustness against the dilepton background. Due to the low statistics of this region, the distribution, as seen in Figure 7, is not very informative.

7 Estimation of Sensitivity

To estimate the sensitivity offered by this analysis without unblinding the analysis, a fit to Asimov data is performed. In this analysis only statistical uncertainties are considered. In [12] it was shown, that the statistical uncertainties are dominant anyway, making this a reasonable approximation. Note, that even though the analysis blinded by shifting the signal sample cross-section by a value of $\sim \pm 10\%$, the fit, however, relies on both shape and normalisation of the signal. The Asimov data is generated by adding up signal and background prediction. The nominal value of a_τ is taking to be 0.0 here, which is given the spacing of the templates of 0.01 the closest value to the SM prediction. The likelihood

Figure 7: Transverse momentum of muon in the SR-1μ1e region.

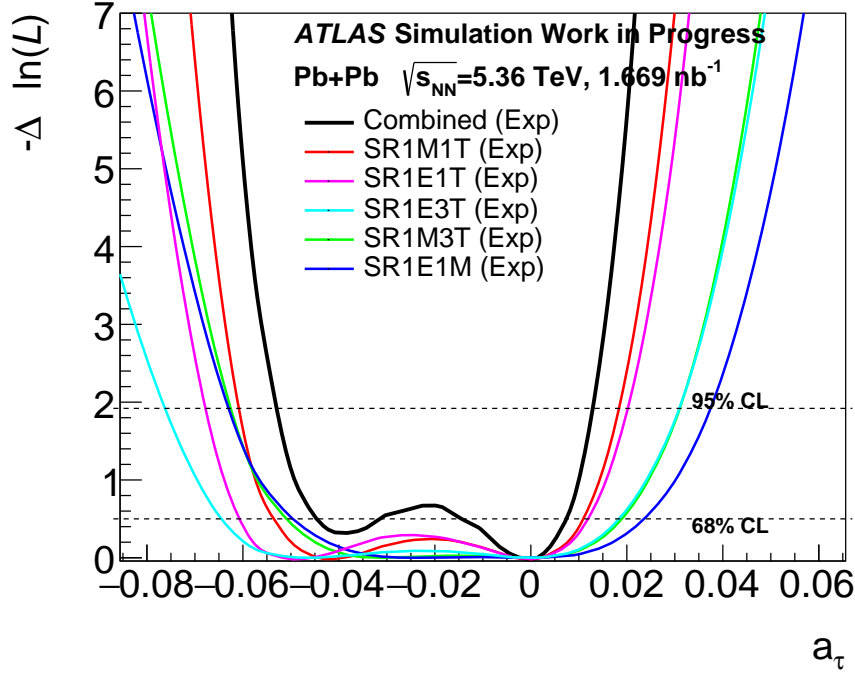Figure 8: Likelihood scan of the Asimov data.
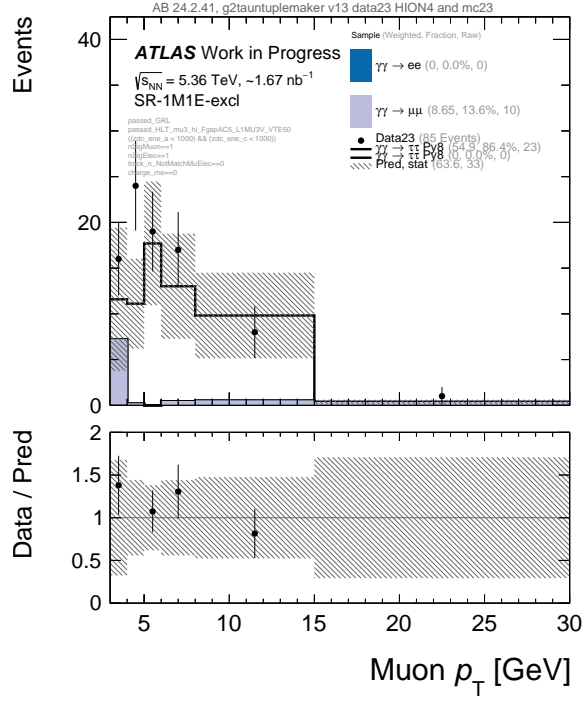
Figure 9: Likelihood scan of the Asimov data, where only the yield of the signal is considered.

scan of the Asimov data is shown in Figure 8. The likelihood scan shows a clear minimum at the nominal value of $a_\tau = 0.0$. The likelihood scan is used to estimate the sensitivity of the analysis. From the shape and the incline of the curves, we can see, which regions prove to be the most sensitive. As one would expect, the SR-$1\ell1$T regions are the most sensitive, as they are the most susceptible to the dilepton background, with the SR-$1\mu1$T region being the most sensitive. The SR-$1\ell3$T regions are less sensitive, despite having a higher signal to background ratio. This is due to the lower statistics of the regions.

Another important feature of the likelihood scan to note is the asymmetric shape of the curve. This can be explained by the cross-section dependence of the signal on a_τ. The cross-section of the signal sample as a function of a_τ is shown in Figure 8. The parabolic shape of the curve introduces a degeneracy in the likelihood scan. This degeneracy can be broken by the a_τ-dependence of the shape of the distribution (See Figure 13), resulting in the asymmetry. The likelihood scan, where only the yield of the signal is considered, is shown in Figure 9. The likelihood scan of the individual regions display a symmetric shape, as expected by the degeneracy of a_τ assigned to the cross-section. The second minimum, however, occurs at a different position for each region. This is due to the different kinematic cuts in each region, leading to a different dependency of the signal cross-section on a_τ. Exemplary is this displayed in Figure 11. This introduces a different position of the second minimum in the likelihood scan for each region.
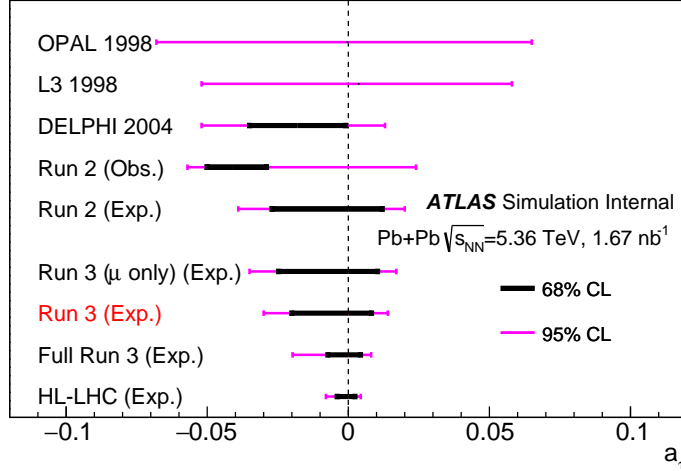
8 Conclusion

Figure 10: Sensitivity of previous measurement of a_τ and the expected sensitivity of this analysis, and the projected sensitivity for higher luminosity scenarios.

The Heavy Ion collision data recorded by ATLAS provides a sensitive environment to probe the anomalous magnetic moment of the tau lepton a_τ. Ultra-peripheral collision provide a high photon flux, enhancing the number of light-by-light scattering events. They further offer a clean event topology, making the signal process accessible in the event selection. Using a template fit of the signal regions, the sensitivity of the analysis is estimated.

The expected sensitivity provided by this analysis is shown in Figure 10. Including the electron signal regions improves the sensitivity of the analysis. Using the current Run 3 data set of $\mathcal{L} = 1.67\,\mathrm{nb}^{-1}$, the analysis is expected to provide the most precise single measurement[1]. The data set provided by the HL-LHC is expected to increase the sensitivity by a factor of 5 compared to the Run 2 analysis by ATLAS. Before the application of this analysis to the event data and the unblinding of the analysis, some further investigation of fluctuations observed in some of the signal regions is necessary. This includes the investigation of a possible missing background in the SR-1e3T region and the normalisation of the dilepton background in the CR-2e region.

This work mostly assumed that the investigation of the background processes in the previous analysis by ATLAS [12] is valid for the electron regions too. In the light of the observed deviations and the expected difference in reconstruction efficiency, a re-evaluation of the background processes in the electron regions is necessary.

---

[1]This does not include a recent analysis published by CMS [13]. Since the analysis has not been published in a journal at the time of writing (01.09.2024), it is not included in this comparison.

9 Acknowledgements

A Cutflows

Requirement	Data 23	$\gamma\gamma \to \tau\tau$	$\gamma\gamma \to ee$	$\gamma\gamma \to \mu\mu$	Pred	B	S/B	$S/\sqrt{S+B}$
pass GRL	1489893.0	69313.0	670874.1	494220.9	1234408.0	1165095.0	0.1	62.4
HLT e- trigger	1090600.0	11238.0	174453.3	57731.4	243422.7	232184.7	0.0	22.8
$E_{\mathrm{ZDC}}^{A,C} < 1$ TeV	532051.0	11238.0	174453.3	57731.4	243422.7	232184.7	0.0	22.8
$N_e^{\mathrm{baseline}} = 2$	101774.0	481.5	79256.2	2.3	79740.1	79258.6	0.0	1.7
$N_e^{\mathrm{sig}} = 2$	53516.0	51.9	45400.1	0.4	45452.3	45400.5	0.0	0.2
$N_{\mathrm{trk}}\ (\Delta R > 0.1$ from $e) = 0$	52553.0	45.3	45325.8	0.0	45371.1	45325.8	0.0	0.2
$m_{ee} > 11$ GeV	23724.0	14.0	20575.6	0.0	20589.6	20575.6	0.0	0.1
$\sum$ charge $= 0$	23662.0	14.0	20515.2	0.0	20529.3	20515.2	0.0	0.1

Table 3: AB 24.2.41, g2tauntuplemaker v13 data23 HION4 and mc23. Control region CR-2E-excl. Normalised to $\mathcal{L} = 1.669$ nb^{-1}.

Requirement	Data 23	$\gamma\gamma \to \tau\tau$	$\gamma\gamma \to ee$	$\gamma\gamma \to \mu\mu$	Pred	B	S/B	$S/\sqrt{S+B}$
pass GRL	1489893.0	69313.0	670874.1	494220.9	1234408.0	1165095.0	0.1	62.4
HLT mu3 trigger	401729.0	1802.6	0.7	79164.4	80967.7	79165.1	0.0	6.3
$E_{\mathrm{ZDC}}^{A,C} < 1$ TeV	109394.0	1802.6	0.7	79164.4	80967.7	79165.1	0.0	6.3
$N_\mu^{\mathrm{baseline}} = 2$	75971.0	145.9	0.0	71775.6	71921.4	71775.6	0.0	0.5
$N_\mu^{\mathrm{sig}} = 2$	60486.0	70.3	0.0	58045.3	58115.7	58045.3	0.0	0.3
$N_{\mathrm{trk}}\ (\Delta R > 0.1$ from $\mu) = 0$	59347.0	70.3	0.0	57965.8	58036.2	57965.8	0.0	0.3
$m_{\mu\mu} > 11$ GeV	29086.0	41.1	0.0	28962.4	29003.5	28962.4	0.0	0.2
$\sum$ charge $= 0$	29085.0	41.1	0.0	28962.4	29003.5	28962.4	0.0	0.2

Table 4: AB 24.2.41, g2tauntuplemaker v13 data23 HION4 and mc23. Control region CR-2M-excl. Normalised to $\mathcal{L} = 1.669$ nb^{-1}.

Requirement	Data 23	$\gamma\gamma \to \tau\tau$	$\gamma\gamma \to ee$	$\gamma\gamma \to \mu\mu$	Pred	B	S/B	$S/\sqrt{S+B}$
pass GRL	1489893.0	69313.0	670874.1	494220.9	1234408.0	1165095.0	0.1	62.4
HLT mu3 trigger	401729.0	1802.6	0.7	79164.4	80967.7	79165.1	0.0	6.3
$E_{\text{ZDC}}^{A,C} < 1$ TeV	109394.0	1802.6	0.7	79164.4	80967.7	79165.1	0.0	6.3
$N_\mu^{\text{baseline}} = 1$	32615.0	1654.5	0.7	6767.5	8422.7	6768.2	0.2	18.0
$N_\mu^{\text{sig}} = 1$	27287.0	1532.1	0.7	5224.3	6757.1	5225.0	0.3	18.6
$N_e^{\text{sig}} = 0$	27094.0	1469.5	0.0	5216.4	6685.9	5216.4	0.3	18.0
N_{trk} ($\Delta R > 0.1$ from μ) $= 1$	6307.0	942.8	0.0	3890.1	4832.9	3890.1	0.2	13.6
Veto unmatched clusters	4688.0	912.5	0.0	3690.1	4602.5	3690.1	0.2	13.5
$\sum$ charge $= 0$	4645.0	894.6	0.0	3683.9	4578.6	3683.9	0.2	13.2
$p_{\text{T}}^{(\mu,\text{trk})} > 1$ GeV	1378.0	836.7	0.0	389.2	1226.0	389.2	2.1	23.9
$p_{\text{T}}^{(\mu,\text{trk},\gamma)} > 1$ GeV	1088.0	785.2	0.0	230.6	1015.9	230.6	3.4	24.6
$p_{\text{T}}^{(\mu,\text{trk,cluster})} > 1$ GeV	992.0	744.9	0.0	205.7	950.7	205.7	3.6	24.2
$A_\phi^{\mu,\text{trk}} < 0.4$	942.0	744.9	0.0	205.4	950.4	205.4	3.6	24.2

Table 5: AB 24.2.41, g2tauntuplemaker v13 data23 HION4 and mc23. Signal region SR-1M1T-excl. Normalised to $\mathcal{L} = 1.669$ nb^{-1}.

Requirement	Data 23	$\gamma\gamma \to \tau\tau$	$\gamma\gamma \to ee$	$\gamma\gamma \to \mu\mu$	Pred	B	S/B	$S/\sqrt{S+B}$
pass GRL	1489893.0	69313.0	670874.1	494220.9	1234408.0	1165095.0	0.1	62.4
HLT e- trigger	1090600.0	11238.0	174453.3	57731.4	243422.7	232184.7	0.0	22.8
$E_{\text{ZDC}}^{A,C} < 1$ TeV	532051.0	11238.0	174453.3	57731.4	243422.7	232184.7	0.0	22.8
$N_e^{\text{sig}} = 1$	104838.0	2224.2	59807.0	16.9	62048.0	59823.9	0.0	8.9
$N_\mu^{\text{sig}} = 0$	104623.0	2129.5	59806.7	0.3	61936.5	59807.0	0.0	8.6
N_{trk} ($\Delta R > 0.1$ from e) $= 1$	54392.0	1386.4	47395.3	0.0	48781.7	47395.3	0.0	6.3
Cluster veto	49162.0	1338.4	45883.2	0.0	47221.6	45883.2	0.0	6.2
$\sum$ charge $= 0$	48688.0	1331.7	45524.6	0.0	46856.2	45524.6	0.0	6.2
$p_{\text{T}}^{(e,\text{trk})} > 1$ GeV	28818.0	1226.9	26870.8	0.0	28097.7	26870.8	0.0	7.3
$p_{\text{T}}^{(e,\text{trk},\gamma)} > 1$ GeV	22024.0	1157.5	19380.8	0.0	20538.3	19380.8	0.1	8.1
$p_{\text{T}}^{(e,\text{trk,cluster})} > 1$ GeV	19225.0	1096.6	16863.5	0.0	17960.1	16863.5	0.1	8.2
$A_\phi^{e,\text{trk}} > 0.012$	2279.0	963.4	859.3	0.0	1822.7	859.3	1.1	22.6

Table 6: AB 24.2.41, g2tauntuplemaker v13 data23 HION4 and mc23. Signal region SR-1E1T-excl. Normalised to $\mathcal{L} = 1.669$ nb^{-1}.

Requirement	Data 23	$\gamma\gamma \to \tau\tau$	$\gamma\gamma \to ee$	$\gamma\gamma \to \mu\mu$	Pred	B	S/B	$S/\sqrt{S+B}$
pass GRL	1489893.0	69313.0	670874.1	494220.9	1234408.0	1165095.0	0.1	62.4
HLT mu3 trigger	401729.0	1802.6	0.7	79164.4	80967.7	79165.1	0.0	6.3
$E_{\mathrm{ZDC}}^{A,C} < 1$ TeV	109394.0	1802.6	0.7	79164.4	80967.7	79165.1	0.0	6.3
$N_\mu^{\mathrm{baseline}} = 1$	32615.0	1654.5	0.7	6767.5	8422.7	6768.2	0.2	18.0
$N_\mu^{\mathrm{sig}} = 1$	27287.0	1532.1	0.7	5224.3	6757.1	5225.0	0.3	18.6
$N_e^{\mathrm{sig}} = 0$	27094.0	1469.5	0.0	5216.4	6685.9	5216.4	0.3	18.0
$N_{\mathrm{trk}} (\Delta R > 0.1$ from $\mu) = 3$	852.0	135.2	0.0	15.3	150.5	15.3	8.8	11.0
Veto unmatched clusters	257.0	131.8	0.0	14.9	146.7	14.9	8.8	10.9
$\sum$ charge $= 0$	212.0	127.3	0.0	14.7	142.1	14.7	8.6	10.7
$m_{\mathrm{trks}} < 1.7$ GeV	137.0	122.8	0.0	5.0	127.8	5.0	24.5	10.9
$A_\phi^{\mu,\mathrm{trks}} < 0.2$	135.0	122.8	0.0	5.0	127.8	5.0	24.5	10.9

Table 7: AB 24.2.41, g2tauntuplemaker v13 data23 HION4 and mc23. Signal region SR-1M3T-excl. Normalised to $\mathcal{L} = 1.669$ nb^{-1}.

Requirement	Data 23	$\gamma\gamma \to \tau\tau$	$\gamma\gamma \to ee$	$\gamma\gamma \to \mu\mu$	Pred	B	S/B	$S/\sqrt{S+B}$
pass GRL	1489893.0	69313.0	670874.1	494220.9	1234408.0	1165095.0	0.1	62.4
HLT e- trigger	1090600.0	11238.0	174453.3	57731.4	243422.7	232184.7	0.0	22.8
$E_{\mathrm{ZDC}}^{A,C} < 1$ TeV	532051.0	11238.0	174453.3	57731.4	243422.7	232184.7	0.0	22.8
$N_e^{\mathrm{sig}} = 1$	104838.0	2224.2	59807.0	16.9	62048.0	59823.9	0.0	8.9
$N_\mu^{\mathrm{sig}} = 0$	104623.0	2129.5	59806.7	0.3	61936.5	59807.0	0.0	8.6
$N_{\mathrm{trk}} (\Delta R > 0.1$ from $e) = 3$	3238.0	207.7	107.9	0.0	315.6	107.9	1.9	11.7
Cluster veto	1043.0	202.5	104.3	0.0	306.8	104.3	1.9	11.6
$\sum$ charge $= 0$	846.0	195.7	100.6	0.0	296.4	100.6	1.9	11.4
$m_{\mathrm{trks}} < 1.7$ GeV	466.0	192.3	78.1	0.0	270.4	78.1	2.5	11.7
$m_{\mathrm{trks}} > 0.5$ GeV	392.0	192.3	40.9	0.0	233.2	40.9	4.7	12.6

Table 8: AB 24.2.41, g2tauntuplemaker v13 data23 HION4 and mc23. Signal region SR-1E3T-excl. Normalised to $\mathcal{L} = 1.669$ nb^{-1}.

Requirement	Data 23	$\gamma\gamma \to \tau\tau$	$\gamma\gamma \to ee$	$\gamma\gamma \to \mu\mu$	Pred	B	S/B	$S/\sqrt{S+B}$
pass GRL	1489893.0	69313.0	670874.1	494220.9	1234408.0	1165095.0	0.1	62.4
HLT mu3 trigger	401729.0	1802.6	0.7	79164.4	80967.7	79165.1	0.0	6.3
$E_{\mathrm{ZDC}}^{A,C} < 1$ TeV	109394.0	1802.6	0.7	79164.4	80967.7	79165.1	0.0	6.3
$N_\mu^{\mathrm{sig}} = 1$	40320.0	1607.6	0.7	16658.0	18266.4	16658.7	0.1	11.9
$N_e^{\mathrm{sig}} = 1$	203.0	62.6	0.3	16.4	79.4	16.8	3.7	7.0
$N_{\mathrm{trk}} (\Delta R > 0.1$ from $\mu/e) = 0$	93.0	57.3	0.0	9.6	66.9	9.6	6.0	7.0
$\sum$ charge $= 0$	85.0	54.9	0.0	8.7	63.6	8.7	6.3	6.9

Table 9: AB 24.2.41, g2tauntuplemaker v13 data23 HION4 and mc23. Signal region SR-1M1E-excl. Normalised to $\mathcal{L} = 1.669$ nb^{-1}.
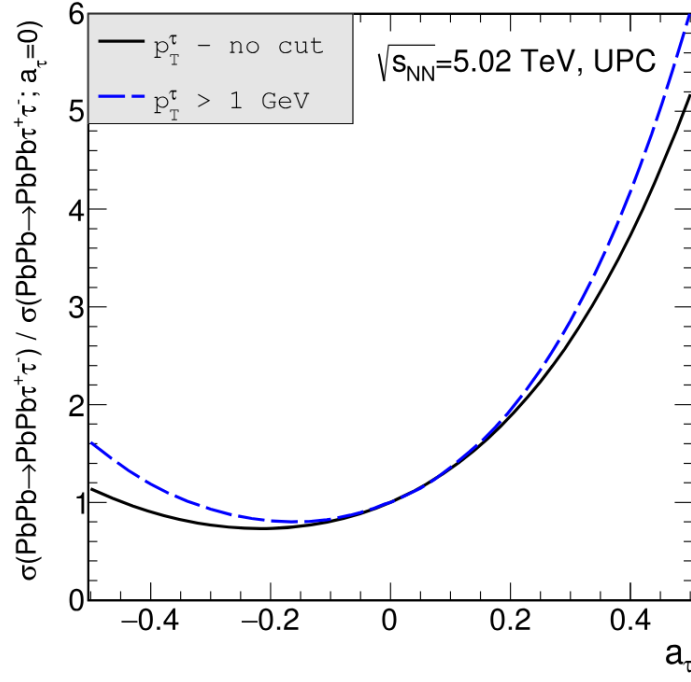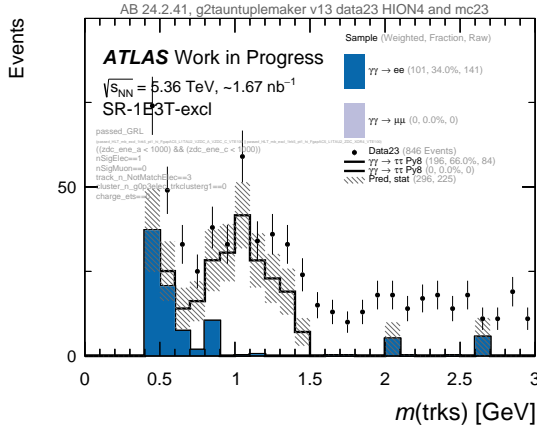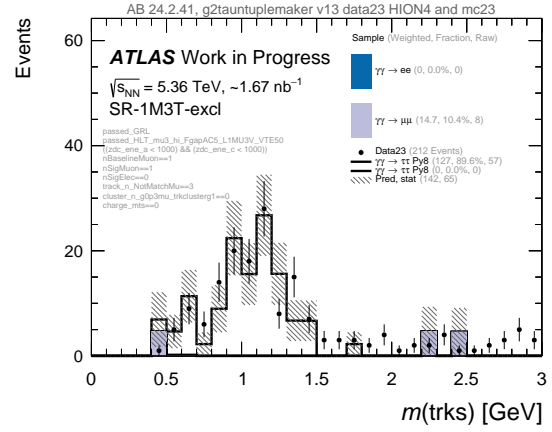
20

B   Plots

Figure 11: Cross section of the signal sample as a function of a_τ. Image taken from [14].

(a) SR-1e3T

(b) SR-1μ3T

Figure 12: Distribution of $p_T(e_1)$ in SR-1ℓ3T before m_{trks} cut
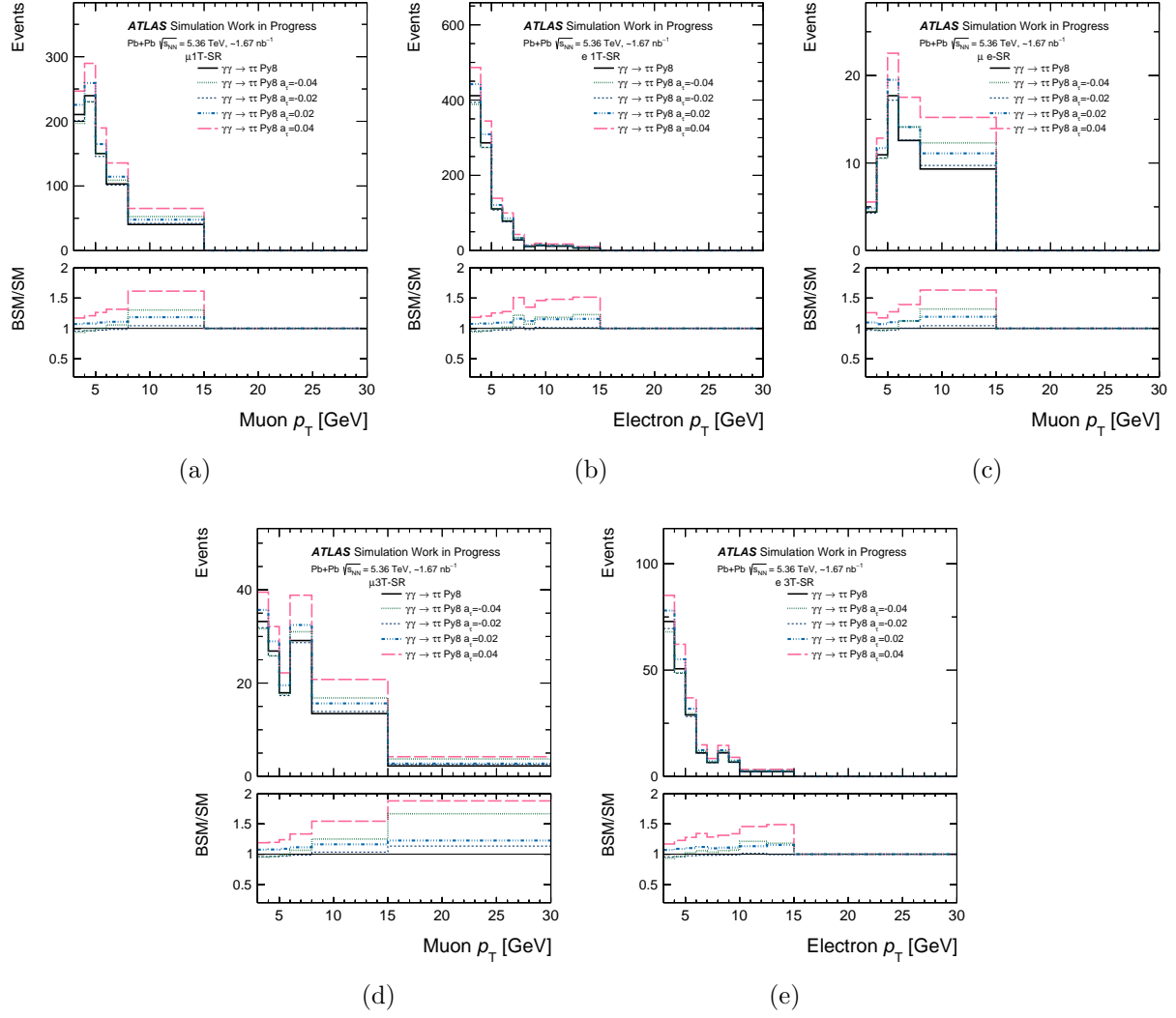
(a)

(b)

(c)

(d)

(e)

Figure 13: Transverse momentum of lepton in the Signal regions.

References

[1] P. A. M. Dirac, *The quantum theory of the electron*, Proceedings of the Royal Society of London. Series A, Containing Papers of a Mathematical and Physical Character **117(778)**, 610 (1928)

[2] J. Schwinger, *On Quantum-Electrodynamics and the Magnetic Moment of the Electron*, Phys. Rev. **73**, 416 (1948)

[3] X. Fan, T. G. Myers, B. A. D. Sukra, G. Gabrielse, *Measurement of the Electron Magnetic Moment*, Phys. Rev. Lett. **130**, 071801 (2023)

[4] T. Aoyama, M. Hayakawa, T. Kinoshita, M. Nio, *Tenth-Order QED Contribution to the Electron $g-2$ and an Improved Value of the Fine Structure Constant*, Phys. Rev. Lett. **109**, 111807 (2012)

[5] The Muon $g-2$ Collaboration, *Measurement of the Positive Muon Anomalous Magnetic Moment to 0.20 ppm*, Phys. Rev. Lett. **131**, 161802 (2023)

[6] S. Eidelmann, M. Passera, *Theory of the τ lepton anomalous magnetic moment*, Modern Physics Letters A **22(03)**, 159 (2007)

[7] DELPHI collaboration, *Study of tau-pair production in photon-photon collisions at LEP and limits on the anomalous electromagnetic moments of the tau lepton*, The European Physical Journal C-Particles and Fields **35(2)**, 159 (2004)

[8] Particle Data Group Collaboration, *Review of Particle Physics*, Phys. Rev. D **110**, 030001 (2024)

[9] S. P. Martin, J. D. Wells, *Muon anomalous magnetic dipole moment in supersymmetric theories*, Phys. Rev. D **64**, 035003 (2001)

[10] ATLAS Collaboration, *High-Luminosity Large Hadron Collider (HL-LHC): Technical design report*, CERN Yellow Reports: Monographs, CERN, Geneva (2020)

[11] ATLAS Collaboration, *The ATLAS Experiment at the CERN Large Hadron Collider*, J. Instrum. **3**, S08003 (2008)

[12] ATLAS Collaboration, *Observation of the $\gamma\gamma \to \tau\tau$ Process in $\mathrm{Pb}+\mathrm{Pb}$ Collisions and Constraints on the τ-Lepton Anomalous Magnetic Moment with the ATLAS Detector*, Phys. Rev. Lett. **131**, 151802 (2023)

[13] CMS Collaboration, *Observation of $\gamma\gamma \to \tau\tau$ in proton-proton collisions and limits on the anomalous electromagnetic moments of the τ lepton* (2024), `2406.03975`, URL `https://arxiv.org/abs/2406.03975`

[14] M. Dyndał, M. Kłusek-Gawenda, A. Szczurek, M. Schott, *Anomalous electromagnetic moments of τ lepton in $\gamma\gamma \to \tau^+\tau^-$ reaction in Pb+Pb collisions at the LHC*, Physics Letters B **809**, 135682 (2020)